Journal of Alloys and Compounds 1055 (2026) 186392

Contents lists available at ScienceDirect

Journal of Alloys and Compounds

journal homepage: www.elsevier.com/locate/jalcom

Void-filling FeNi interface engineering for loss suppression in Fe-based nanocrystalline composites

Dong Li [1], Yanzhou Fan [1], Min Wang, Changlong Jin, Jiayi Huang, Zhe Jia, Qianqian Wang, Qiang Luo [*], Zhijun Guo [*], Baolong Shen

School of Materials Science and Engineering, Jiangsu Key Laboratory for Advanced Metallic Materials, Southeast University, Nanjing 211189, China

ARTICLE INFO

Keywords:
Fe-based nanocrystalline composites
$Fe_{50}Ni_{50}$ doping
Soft magnetic properties
Core loss
Domain dynamics
High-frequency performance

ABSTRACT

This study explores the enhancement of Fe-based nanocrystalline soft magnetic composites (SMCs) through the introduction of phosphated $Fe_{50}Ni_{50}$ particles into the FeCoSiBPCCuNb matrix. $Fe_{50}Ni_{50}$ was chosen due to its high saturation magnetic induction intensity, low magnetocrystalline anisotropy, and ability to improve densification by filling interstitial voids within the matrix. The 5 wt% $Fe_{50}Ni_{50}$-doped SMCs exhibit remarkable performance with effective permeability (μ_e) ≈ 60 (stable from 1 kHz to 20 MHz) and ultra-low core loss (P_{cv} = 2441 mW/cm^3) at 0.05 T, 1 MHz. These values significantly outperform traditional Fe-based SMCs. The performance enhancement is attributed to $Fe_{50}Ni_{50}$'s role in reducing porosity and enhancing interparticle magnetic coupling, which improves domain-wall motion. Loss separation analysis reveals that at low $Fe_{50}Ni_{50}$ concentrations, P_{cv} is reduced due to improved packing and the elimination of large voids. However, at higher $Fe_{50}Ni_{50}$ contents (≥10 wt%), particle agglomeration introduces interfacial pinning sites, leading to increased hysteresis loss (P_h). Frequency-dependent analysis shows that dynamic domain processes dominate at higher frequencies, with excess loss (P_{exc}) becoming the primary contributor. This work demonstrates that $Fe_{50}Ni_{50}$ doping offers a scalable and effective method for achieving high-frequency, low-loss soft magnetic materials, with potential applications in power electronics and high-efficiency inductive components.

1. Introduction

Soft magnetic materials are indispensable in power electronic devices, where the simultaneous realization of high saturation magnetic induction intensity (B_s), high effective permeability (μ_e), and low core loss (P_{cv}) is crucial[1,2]. Among them, soft magnetic composites (SMCs) based on Fe-based nanocrystalline alloys have drawn significant attention because of their superior comprehensive performance under high-frequency and complex operating conditions [3]. However, the limited amorphous-forming ability of Fe-based nanocrystalline SMCs restricts the achievable iron content[4–6]. As a result, current Fe-based nanocrystalline SMCs exhibit lower B_s than high-flux magnetic SMCs [7], and higher P_{cv} than ferrite[8,9], preventing their widespread use in next-generation high-power-density devices. Several strategies have been explored to address these limitations. Increasing the iron content can raise B_s, but this degrades the amorphous forming ability of matrix [10], causing uniformly sized α-Fe to form during annealing and leading to severe P_{cv} during the annealing process [11]. Applying insulation coatings, such as phosphoric acid treatment, can form a dense phosphate coating on the surface of the powder, reduces the high-frequency P_{cv}, but usually lowers B_s[12,13]. Increasing compaction pressure enhances density and moderately raises B_s, yet excessive pressure fractures the particles and damages the insulation layer, which in turn increases P_{cv}[14]. These approaches highlight the persistent challenge of simultaneously achieving high B_s and low P_{cv}.

Powder doping has emerged as one of the most promising routes to overcome this trade-off. High-B_s dopants such as reduced iron powder, FeSi powder, and carbonyl iron powder (CIP) improve B_s but inevitably cause significant increases in P_{cv}[15–17]. For example, Wang [18] et al. demonstrated that CIP-doped $Fe_{73.5}Si_{13.5}B_9Cu_1Nb_3$ SMCs exhibits enhanced B_s but markedly worsened P_{cv} at 300 kHz, with deterioration becoming more severe at higher CIP content. Similarly, Shi [19] et al. observed that reduced iron doping increased B_s but led to a higher P_{cv} across 100 kHz to 1 MHz. These findings demonstrate that traditional

* Corresponding authors.
E-mail addresses: q-luo@seu.edu.cn (Q. Luo), zj-guo@seu.edu.cn (Z. Guo).
[1] These authors contribute equally to this work as co-first authors

https://doi.org/10.1016/j.jallcom.2026.186392
Received 10 November 2025; Received in revised form 1 January 2026; Accepted 22 January 2026
Available online 24 January 2026

doping strategies cannot resolve the intrinsic conflict between B_s and P_{cv}. $Fe_{50}Ni_{50}$ represent a more effective solution, combining high B_s (~1.58 T), high μ_e, and low magnetocrystalline anisotropy, making them uniquely suited for improving both density and magnetic performance. Their intrinsic ductility allows small $Fe_{50}Ni_{50}$ powders to fill voids, reduce porosity and increase compaction density, which directly suppresses P_{cv} [20–22]. Nevertheless, existing studies on $Fe_{50}Ni_{50}$ doping have not achieved satisfactory results. Feng [23] et al. showed that doping a $Fe_{73.5}Si_{13.5}B_9Cu_1Nb_3$ matrix with 50 wt% FeNi improved B_s and reduced P_{cv} within 100 kHz to 1 MHz, but the saturation magnetization (M_s) was still limited (136.3 emu/g) and P_{cv} remained as high as 599 mW/cm^3 (at 0.05 T, 200 kHz). Moreover, the untreated $Fe_{50}Ni_{50}$ powder will enhance the conductive path and bring about large P_{cv} at high frequency. Chen [24] et al. also achieved similar improvements by doping $Fe_{83.5}Si_{7.5}B_5Cr_4$ powder with 15 wt% FeNi. However, due to the limitation of the properties of the matrix itself, the P_{cv} of 72.5 W/kg (at 0.04 T, 200 kHz) is still too high for industrial applications. Therefore, in order to obtain high-performance SMCs, it is necessary to select high-performance matrix powder and insulation treated $Fe_{50}Ni_{50}$ powder.

In our previous work, we developed a FeCoSiBPCCuNb nanocrystalline SMCs with B_s of 0.99 T and P_{cv} of 110 mW/cm^3 at 0.05 T, 100 kHz, demonstrating a strong baseline for high-frequency applications. To meet the demands of industrial scenarios, further enhancement of B_s is required. In the present study, phosphated $Fe_{50}Ni_{50}$ powder is introduced into the FeCoSiBPCCuNb to fabricate doped soft magnetic composites (DSMCs). In order not to sacrifice the B_s of the matrix powder, only the $Fe_{50}Ni_{50}$ powder was phosphatized. By carefully optimizing the $Fe_{50}Ni_{50}$ content, we reveal how doping simultaneously enhances B_s and reduces P_{cv}, and mitigates the longstanding trade-off. The sample optimized with 5 wt% phosphated $Fe_{50}Ni_{50}$ achieves a B_s of 1.03 T and a P_{cv} of only 86 mW/cm^3 at 0.05 T, 100 kHz and 2441 mW/cm^3 at 0.05 T, 1 MHz. These results demonstrate that $Fe_{50}Ni_{50}$ doping is not only an effective pathway to overcome the performance bottleneck of Fe-based nanocrystalline SMCs, but also a practical strategy for designing high-frequency, high-power-density electronic devices.

2. Materials and methods

High-purity Fe, Co, Si, B, Nb, Cu (all with purity >99.99 %) and FeP and FeC alloys were weighed according to atomic ratios and melted by induction melting under a high-purity argon atmosphere to produce alloy ingot with the nominal composition $(Fe_{0.74}Co_{0.04}Si_{0.09}B_{0.08}P_{0.05}C_{0.02})_{97.7}Cu_{0.8}Nb_{1.5}$. Alloy powders were then prepared by gas atomization and sieved through a 270-mesh screen to obtain the FeCoSiBPCCuNb powder. The $Fe_{50}Ni_{50}$ alloy powders were produced by Fujia Technology (Hunan, China) and possesses a sphericity greater than 90 %. $Fe_{50}Ni_{50}$ powder was introduced into a phosphoric acid solution (at a weight of 1 % relative to the powder mass, dissolved in acetone). The mixture was dispersed ultrasonically for 10 min to ensure homogeneity, and stirring continuously at 60 °C until the powder dried, hence forming a phosphate insulating layer on the powder surface. Then, it was uniformly mixed with FeCoSiBPCCuNb powder using a QM3SP04L planetary ball mill. The ball milling time was 0.5 h and the rotational speed was 150 rotations per minute. Its primary purpose is to achieve uniform dispersion of small $Fe_{50}Ni_{50}$ powders in the matrix. Subsequently, 2 wt% epoxy resin dissolved in acetone was added to coat the mixed powders, followed by stirring until the acetone fully evaporated. The processed powders were compacted by cold-pressed under 1800 MPa for 60 s into toroidal samples with an outer diameter of 12.7 mm and an inner diameter of 7.6 mm. Finally, the compacts were annealed at 510 °C for 30 min under vacuum to form nanocrystalline. Based on phosphated $Fe_{50}Ni_{50}$ content, the powders and their corresponding DSMCs were designated as 0, 5, 10, 15, and 20 wt% $Fe_{50}Ni_{50}$. The overall fabrication process is schematically illustrated in Fig. 1.

Phase structure of FeCoSiBPCCuNb, $Fe_{50}Ni_{50}$ powders, and the DSMCs were characterized by X-ray diffraction (XRD, Bruker D8 Discover) with Cu-Kα radiation. The particle size and distribution of the raw powders were measured using a laser particle size analyzer (LPSA, Microtrac S3500). Morphology and elemental distributions of powders and DSMCs were examined using scanning electron microscopy (SEM, Zeiss Crossbeam 350) coupled with energy-dispersive spectroscopy (EDS). Magnetic hysteresis loops of DSMCs were measured using a vibrating sample magnetometer (VSM, Lake Shore 7407). Electrical resistivity was measured with a high-resistance microcurrent tester (ST2643, Suzhou Jingge). The density and open porosity of the DSMCs

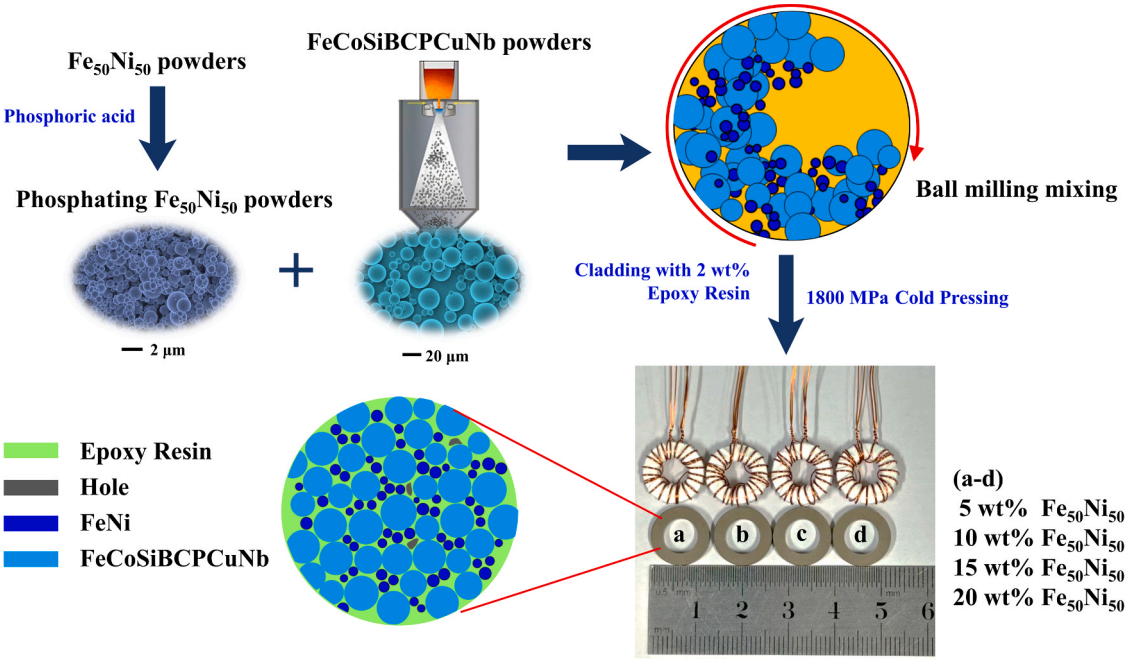

Fig. 1. Experimental flowchart for the preparation of FeCoSiBPCCuNb/$Fe_{50}Ni_{50}$ DSMCs.

was measured by the Archimedes' principle. μ_e was measured using an impedance analyzer (E4990A, Agilent), while P_{cv} was evaluated using a B-H analyzer combined with a power amplifier (HSA4014-IW, SY-8218, IWATSU, Japan). DC-bias characteristics were measured with a wide-band LCR tester and DC-current source (TH2839 and TH1778A, Changzhou Tonghui).

3. Result and discussion

Representative morphologies of the $Fe_{50}Ni_{50}$ and FeCoSiBPCCuNb powders are shown in Fig. 2 **(a, b).** The $Fe_{50}Ni_{50}$ powders exhibit predominantly spherical or near-spherical particles with a relatively narrow size distribution centered around 2 μm. The FeCoSiBPCCuNb powders also display a regular spherical morphology, characteristic of gas atomization. The particle surfaces of both powders appear smooth and free of defects or irregular growths, which is beneficial for reducing friction and agglomeration during processing, thereby improving flowability and compaction behavior. The corresponding particle size distributions (Fig. 2 **(c, d)**) indicate median particle size ($D50$) of ~ 2.1 μm for $Fe_{50}Ni_{50}$ powders and ~24 μm for FeCoSiBPCCuNb powders. Under conditions of closest packing, the larger particles (diameter D) can be filled by smaller particles (diameter d) if diameter ratios (d/D) do not exceed 0.225 [25]. In this study, the ratio of $Fe_{50}Ni_{50}$ to FeCoSiBPCCuNb alloy powders is ~0.085, confirming that the smaller $Fe_{50}Ni_{50}$ particles effectively occupy the interstitial voids among FeCoSiBPCCuNb particles. This packing structure enhances the overall compaction density and reduces porosity, which collectively improve the structural integrity and magnetic performance of the DSMCs.

The phase structure of the powders was examined by XRD, as shown in Fig. 3. In Fig. 3 **(a),** the diffraction peaks of $Fe_{50}Ni_{50}$ powder located at the (111), (200) and (220) planes correspond to an FCC-FeNi structure. Fig. 3 **(b)** shows the XRD patterns of the DSMCs with different phosphated $Fe_{50}Ni_{50}$ contents. For the undoped samples, three peaks at approximately $2\theta = 44.5°$, 66°and 82.3° are indexed to (110), (200) and (211) planes of the α-Fe(Co) phase [26,27], indicating the precipitation of α-Fe(Co) nanocrystals from the amorphous matrix. Upon $Fe_{50}Ni_{50}$ incorporation, only the diffraction peaks of α-Fe(Co) and FCC-FeNi phases are detected. This confirms that no intermetallic or oxide phases form, indicating that the doping process does not induce other phases. As $Fe_{50}Ni_{50}$ content increases from 5 to 20 wt%, the relative intensities of FeNi peaks progressively rise, consistent with the rule of mixtures and uniform phase distribution within the composite. The magnetic hysteresis loops of the DSMCs with different $Fe_{50}Ni_{50}$ doping levels are displayed in Fig. 4. The undoped sample exhibits B_s of 0.99 T. With $Fe_{50}Ni_{50}$ doping up to 15 wt%, B_s increases to ~1.07 T, attributed to the higher B_s of $Fe_{50}Ni_{50}$ (≈1.58 T). However, at 20 wt% doping, B_s decreases slightly, which can be ascribed to the agglomeration of $Fe_{50}Ni_{50}$ particles, leading to local inhomogeneity and reduced compaction density. These observations confirm that moderate $Fe_{50}Ni_{50}$ doping effectively enhances B_s without compromising the phase integrity of the Fe-based nanocrystalline matrix.

Fig. 5 **(a)** shows the μ_e of the DSMCs with different $Fe_{50}Ni_{50}$ contents over the frequency range of 1 kHz to 50 MHz. In particular, the μ_e of 100 wt% $Fe_{50}Ni_{50}$ exhibited a relatively low μ_e of ~ 32, lower than DSMCs. With increasing $Fe_{50}Ni_{50}$ content from 0 to 15 wt%, μ_e gradually increase from 56 to 68, reaching its maximum at 15 wt% due to the void filling densification [28]. According to Visser's non-magnetic boundary model [29]:

$$\mu_e = \frac{\mu_i d}{\mu_i \delta + d} \tag{1}$$

where μ_i is the intrinsic permeability, d is the average particle size, and δ is the fraction of non-magnetic pores. As $Fe_{50}Ni_{50}$ particles progressively fill interstitial voids, δ decreases, thereby increasing μ_e. Samples containing ≤ $Fe_{50}Ni_{50}$ 10 wt% maintain stable μ_e up to ~20 MHz, whereas higher doping levels cause a sharper decline. At 20 wt% doping,

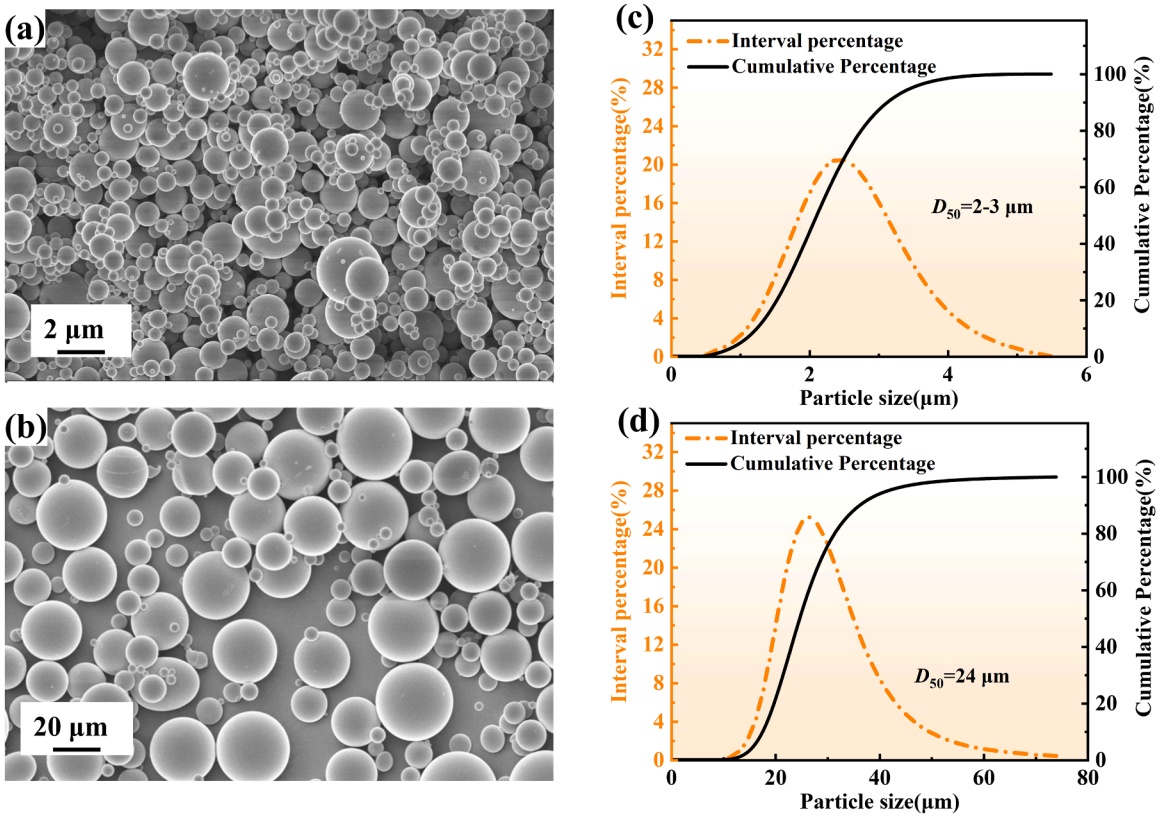

Fig. 2. SEM images of (a) $Fe_{50}Ni_{50}$ powders, (b) FeCoSiBPCCuNb powders, particle size distributions of (c) $Fe_{50}Ni_{50}$ and (d) FeCoSiBPCCuNb powders.

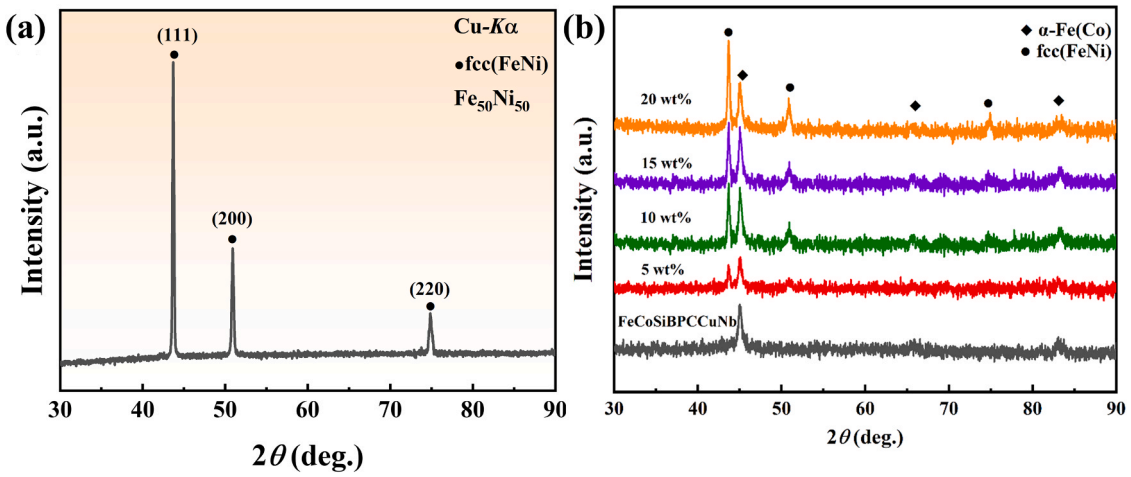

Fig. 3. (a) XRD pattern of $Fe_{50}Ni_{50}$ powders and (b) XRD patterns of DSMCs with different $Fe_{50}Ni_{50}$ doping contents.

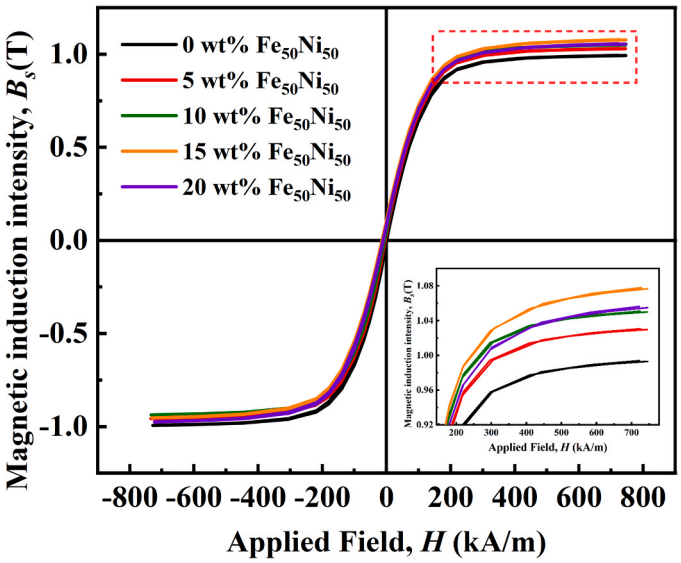

Fig. 4. Hysteresis loops of DSMCs with different $Fe_{50}Ni_{50}$ doping contents.

however, μ_e decreases markedly above 1 MHz, attributed to $Fe_{50}Ni_{50}$ particle agglomeration [30]. This agglomeration enhances the conductive pathways between particles and alters the damping coefficient, transforming the decay pattern of μ_e from resonant to relaxational [31]. Fig. 5 **(b)** illustrates the DC-bias performance of the DSMCs. As DC-bias field increases, the percentage of μ_e in all samples gradually decreases due to progressive saturation. $Fe_{50}Ni_{50}$ doping markedly improve the DC-bias performance. The undoped sample shows a rapid μ_e drop at 100 Oe, while 20 wt% $Fe_{50}Ni_{50}$ DSMCs retains ~62 % of its μ_e at 100 Oe. This enhancement can be attributed to two factors: (i) The addition of $Fe_{50}Ni_{50}$ raises B_s of the DSMCs, making them more resistant to reaching saturation [32]. (ii) $Fe_{50}Ni_{50}$ inherently has excellent DC-bias performance. When a DC-bias field is applied, its μ_e is relatively insensitive to the change of magnetic field before reaching saturation [33]. Consequently, $Fe_{50}Ni_{50}$ doping effectively enhances the DC-bias performance of DSMCs.

The P_{cv} is an important magnetic parameter for nanocrystalline SMCs used in power electronics applications. Fig. 6 shows the frequency dependence of P_{cv} for DSMCs with varying $Fe_{50}Ni_{50}$ contents. As frequency increases, P_{cv} of DSMCs shows a monotonic rise across all samples. Notably, with increasing $Fe_{50}Ni_{50}$ content from 0 to 20 wt%, P_{cv} first decreases and then increases, reaching a minimum at 5 wt% $Fe_{50}Ni_{50}$ at B_m= 0.05 T and 0.1 T, the 5 wt% $Fe_{50}Ni_{50}$ DSMCs exhibits the lowest P_{cv} over 20 kHz to 1 MHz. At 1 MHz, the P_{cv} remains exceptionally low (2441 mW/cm^3 at 0.05 T and 11170 mW/cm^3 at 0.1 T), demonstrating remarkable high-frequency P_{cv} suppression. Importantly, the 5 wt% $Fe_{50}Ni_{50}$-doped DSMCs demonstrates an excellent balance of properties, combining the highest μ_e (~ 60, stable from

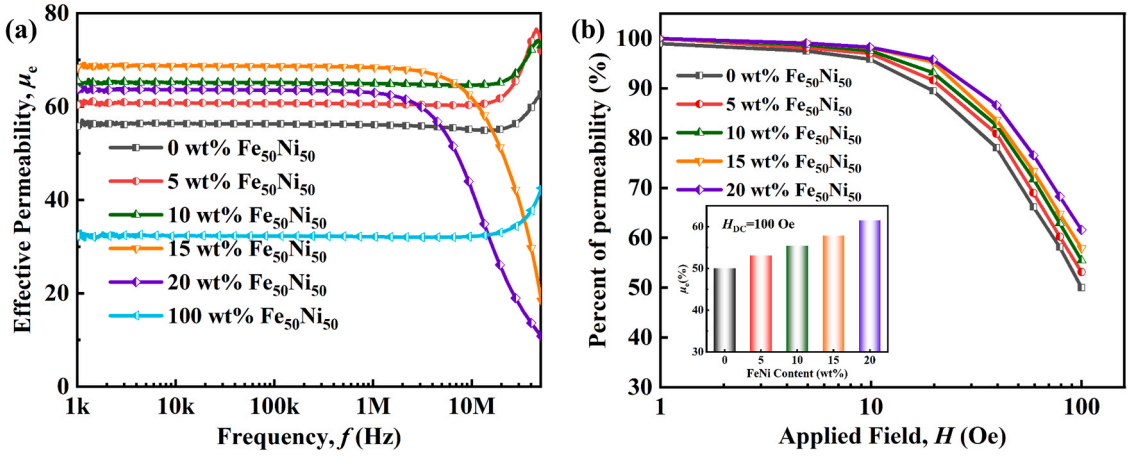

Fig. 5. Frequency characteristics of DSMCs with different $Fe_{50}Ni_{50}$ contents: (a) effective permeability (μ_e) as a function of frequency, and (b) DC-bias performance under various applied field, inset is percentage of μ_e at 100 Oe.

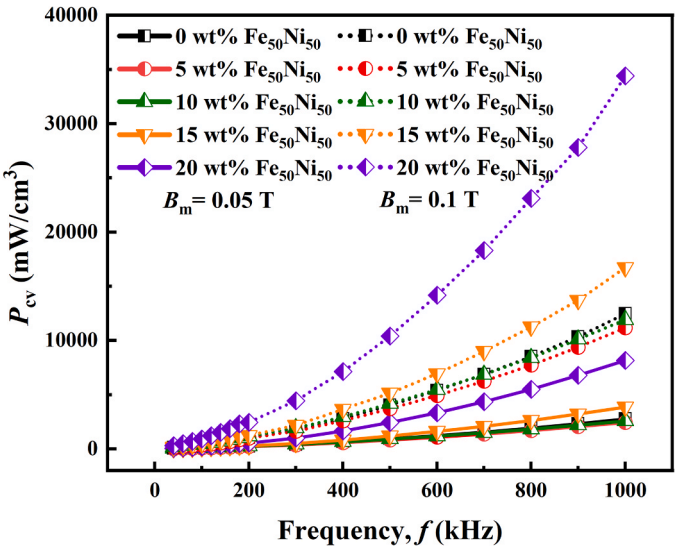

Fig. 6. Frequency dependence of core loss (P_{cv}) for DSMCs with different $Fe_{50}Ni_{50}$ contents at magnetic flux density of 0.05 T and 0.1 T.

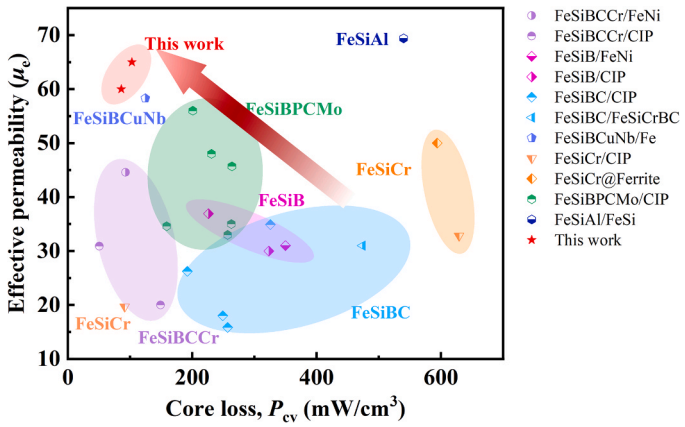

Fig. 7. Comparison of core loss (P_{cv}, 0.05 T, 100 kHz) and effective permeability (μ_e at 1 kHz) between the present DSMCs and previously reported doped magnetic powders.

1 kHz to 20 MHz) with ultra-low P_{cv} (86 mW/cm^3 at 0.05 T, 100 kHz).

The comprehensive properties of DSMCs with different $Fe_{50}Ni_{50}$ doping contents are summarized in Table 1. By balancing B_s, μ_e, DC-bias performance, and P_{cv}, the sample with 5 wt% $Fe_{50}Ni_{50}$ doping exhibits the most favorable combination of soft magnetic properties. Fig. 7 benchmarks these results against previously reported Fe-based DSMCs [16,18,19,23,34–46]. Doping with high-B_s particles is a common strategy for enhancing magnetic properties, but its effectiveness varies significantly depending on the doping content and the properties of the matrix. The present DSMCs clearly outperform prior systems, achieving a superior combination of high μ_e and low P_{cv}. This advancement underscores the effectiveness of $Fe_{50}Ni_{50}$ doping in FeCoSiBPCCuNb matrices for simultaneously enhancing μ_e and reducing high-frequency P_{cv}, offering a practical route toward next-generation high-frequency SMCs.

The structural compactness and compositional homogeneity of the DSMCs provide a physical foundation for understanding their magnetic behavior. As shown in Fig. 8, the undoped SMCs (0 wt% $Fe_{50}Ni_{50}$) exhibits significant internal porosity due to insufficient packing, yielding the lowest density (5.37 g/cm^3) and the highest porosity (12.3 %). These voids act as non-magnetic defects that dilute the magnetic phases, hinder domain wall motion, and introduce additional pinning centers, which directly linked to the reduced μ_e and elevated P_{cv} observed earlier. Introducing $Fe_{50}Ni_{50}$ powders markedly alters this microstructure. With doping levels of 5–15 wt%, the $Fe_{50}Ni_{50}$ powders efficiently fill the voids among the FeCoSiBPCCuNb powders, leading to densification (Fig. 8 **(f)**). The bulk density consequently rises from 5.45 to 5.54 g/cm^3 and the porosity decreases from ~10.6 % to ~9.5 %, while the micrographs reveal a more compact and uniformly bonded structure. This densification minimizes non-magnetic interfaces, promotes smooth domain wall motion, and ultimately leads to enhanced μ_e and reduced P_{cv}. When the $Fe_{50}Ni_{50}$ content reaches 20 wt%, however, excessive small particles tend to agglomerate (Fig. 8 **(e)**), creating localized clusters that introduce porosity and disrupt the uniform packing of the matrix. The resulting decrease in density to 5.46 g/cm^3 and the porosity rebounds to 10.2 %, and this partial P_{cv} of magnetic continuity explain the deterioration in soft magnetic properties at higher doping levels.

Elemental mapping further corroborates this structural evolution (Fig. 9). The Ni signal, serving as the tracer for $Fe_{50}Ni_{50}$, clearly reveals the evolution of particle dispersion with doping level. In the optimal 5 wt% sample, Ni is sparse and uniformly dispersed, indicating that the $Fe_{50}Ni_{50}$ particles act as discrete fillers within the matrix. At 10–15 wt%, the Ni distribution becomes more continuous and homogeneous, suggesting enhanced filling of interstitial voids. However, at 20 wt% $Fe_{50}Ni_{50}$, although the overall distribution remains macroscopically uniform, localized regions of high Ni concentration emerge. This local compositional clustering interrupts magnetic-flux continuity, providing direct chemical evidence for the origin of the slight decline in B_s and μ_e at high doping levels.

The evolution of P_{cv} in the DSMCs reveals a complex interplay among structural densification, interfacial coupling, and dynamic domain processes. Bertotti loss separation model was used in this study for P_{cv} separation. As depicted in Fig. 10 **(a, b)**, hysteresis loss (P_h) exhibits a non-monotonic dependence on $Fe_{50}Ni_{50}$ content and it is strongly correlated with coercivity (H_c). Increasing $Fe_{50}Ni_{50}$ from 0 wt% to 5 wt %, markedly lowers P_h (from 1576 to 1487 mW/cm^3 at 0.05 T, 1 MHz), H_c also decreased accordingly, which is arises from optimized interstitial filling and minimized pinning. The improvement in packing density minimizes non-magnetic discontinuities and promotes smoother magnetization reversal. With further $Fe_{50}Ni_{50}$ doping (10–15 wt%), however, P_h rises again despite the continued increase in density (Fig. 8 **(f)**). This phenomenon primarily occurs because the drawbacks of agglomeration outweigh the benefits of high density, resulting in elevated P_h levels. It originates from the proliferation of $Fe_{50}Ni_{50}$/matrix interfaces that introduce additional pinning sites. Fig. 10 **(c)** shows the

Table 1
Summary of magnetic properties for DSMCs with different $Fe_{50}Ni_{50}$ contents.

$Fe_{50}Ni_{50}$ content (wt%)	B_s (T)	μ_e 1 kHz	DC-bias (%) 100 Oe	P_{cv} (mW/cm^3) 0.05 T		P_{cv} (mW/cm^3) 0.1 T	
				200 kHz	1 MHz	200 kHz	1 MHz
0	0.99	56	50	239	2770	451	12470
5	1.03	60	53	220	2441	448	11170
10	1.05	66	55	253	2577	562	11910
15	1.07	68	58	282	3863	604	16720
20	1.05	64	62	546	8164	1220	34390

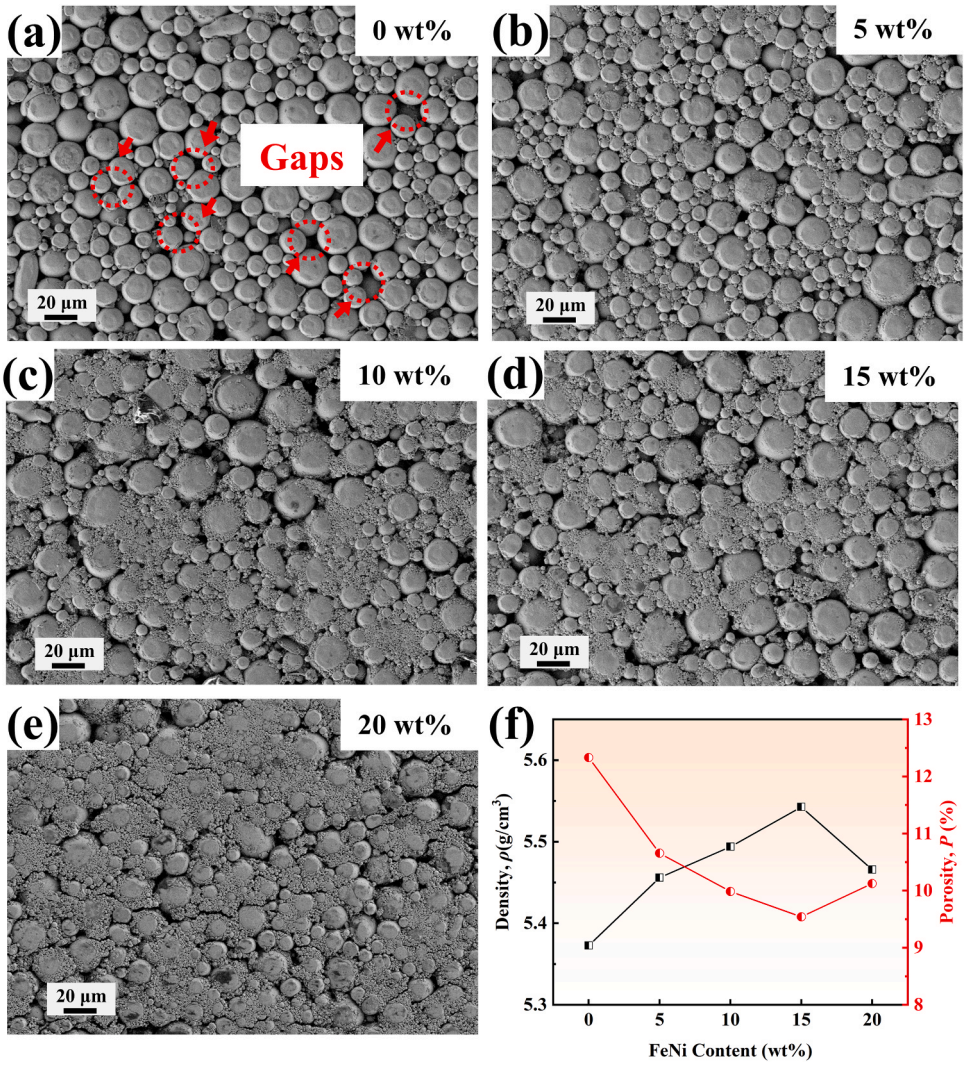

Fig. 8. (a–e) Cross-sectional microstructures and (f) corresponding density and porosities of DSMCs with different $Fe_{50}Ni_{50}$ doping contents.

resistivity with different $Fe_{50}Ni_{50}$ content, observing a monotonically decreasing trend. This is attributed to the inherently low resistivity of $Fe_{50}Ni_{50}$ powder. The behavior of eddy current loss (P_e, Fig. 10 **(d, e)**) mirrors a delicate balance between two competing mechanisms. On the microscale, the inclusion of small $Fe_{50}Ni_{50}$ particles decrease the average particle size and suppress intra-particle eddy currents loss ($P_{e\text{-}intra}$), decreasing from 597 mW/cm^3 for undoped to 479 mW/cm^3 for 20 wt% $Fe_{50}Ni_{50}$ (0.05 T, 1 MHz). Conversely, the conductive $Fe_{50}Ni_{50}$ network establishes inter-particle pathways that lower bulk resistivity and elevate inter-particle eddy currents loss ($P_{e\text{-}inter}$), increasing from 70 mW/cm^3 for undoped to 190 mW/cm^3 for 20 wt% $Fe_{50}Ni_{50}$ (0.05 T, 1 MHz). Within the 1 MHz frequency range, these two effects largely compensate each other, yielding an almost constant total P_e across compositions. Excess loss (P_{exc}), primarily related to the motion of domains and cutoff frequency, is also strongly correlated with pinning sites [47,48]. Therefore, $Fe_{50}Ni_{50}$ doping mainly affects P_{exc} through changing the number of pinning sites. In addition, P_{exc} is also scales with core density and the volume fraction of non-magnetic phase [36]. Consequently, P_{exc} follow the similar trend as P_h, reaching its minimum at 5 wt% $Fe_{50}Ni_{50}$ content, where interfacial pinning minimized (Fig. 10 **(f)**).

Frequency-resolved loss separation (Fig. 11) further clarifies these relationships. At 200 kHz, the P_h dominates total P_{cv}, while P_e and P_{exc} contribute marginally. In this regime, $Fe_{50}Ni_{50}$ primarily influences P_h through its effect on structural density. As the frequency increases to 1 MHz, the balance shifts: P_{exc} rises sharply and becomes the dominant component, particular in heavily doped samples, signifying that high-frequency P_{cv} is governed by dynamic domain interactions rather than eddy currents [49,50].

The mechanistic insights of DMSCs are summarized schematically in Fig. 12**.** In the undoped state, internal voids and discontinuous magnetic paths yield high P_{cv}. Moderate $Fe_{50}Ni_{50}$ addition (5 wt%) fills interstitial voids, improves densification, thereby reducing the resistance of domain wall motion, collectively reducing P_h and P_{exc} while maintaining low P_e. Beyond the optimal level, excessive $Fe_{50}Ni_{50}$ induces particle clustering and interfacial accumulation, which elevate eddy-current pathways. These new interfaces become additional pinning sites, hindering domain wall movement and leading to the increase of P_{exc}. Consequently, the P_{cv} minima shift upward again. This hierarchical model rationalizes the observed non-monotonic evolution of P_{cv} and highlights the crucial role of controlled $Fe_{50}Ni_{50}$ incorporation in maintaining low-loss performance across MHz frequencies.

4. Conclusion

This work presents a novel approach to enhancing the performance of Fe-based nanocrystalline SMCs by introducing phosphated $Fe_{50}Ni_{50}$ powders into the FeCoSiBPCCuNb matrix. $Fe_{50}Ni_{50}$ was chosen for its high B_s, low magnetocrystalline anisotropy, and unique ability to improve the densification of the composite, resulting in significant

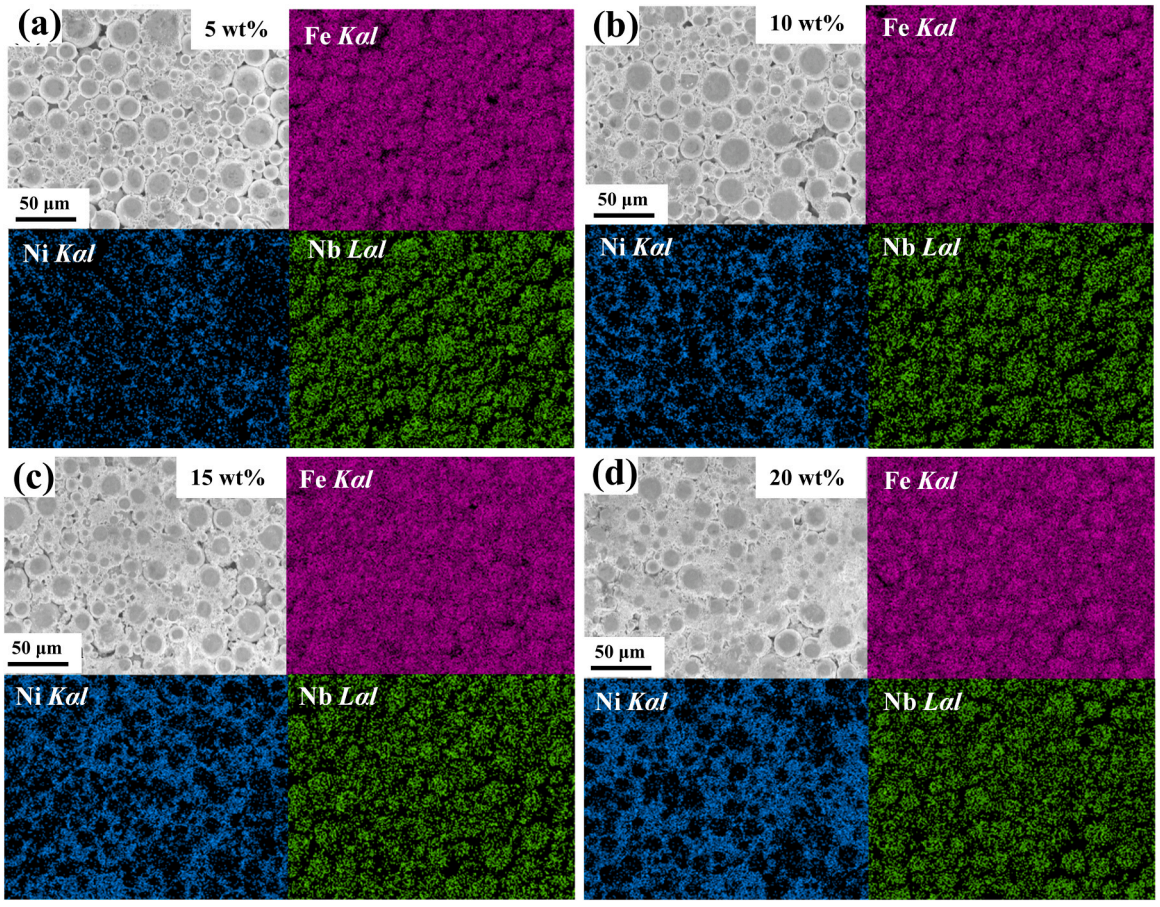

Fig. 9. Cross-sectional SEM images and EDS elemental mappings of Fe, Ni, and Nb for DSMCs containing different $Fe_{50}Ni_{50}$ doping levels.

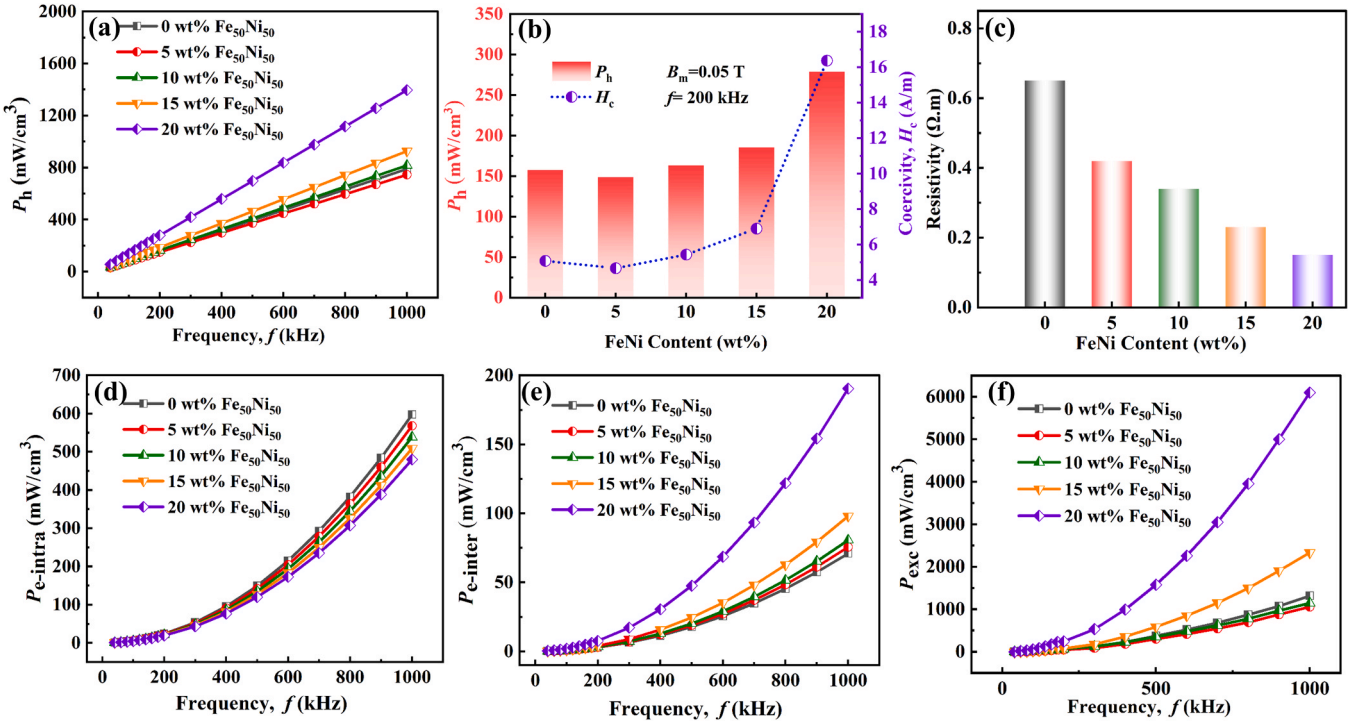

Fig. 10. (a) hysteresis loss, (b) correlation between hysteresis loss and coercivity at B_m = 0.05 T, 200 kHz, (c) resistivity, (d) intra-particle eddy current loss, (e) inter-particle eddy current loss and (f) excess loss of DSMCs with different $Fe_{50}Ni_{50}$ contents.

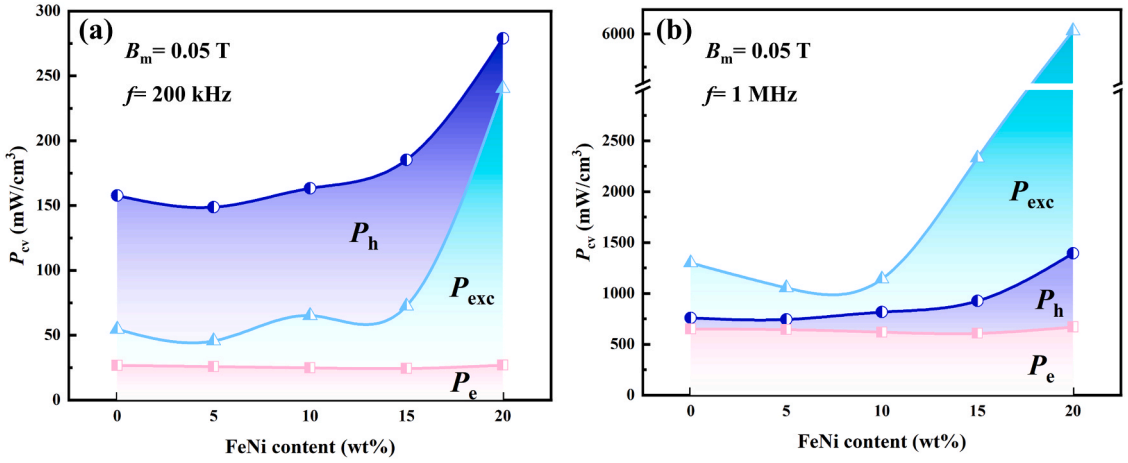

Fig. 11. Contributions of different loss components to the P_{cv} of DSMCs at (a) 0.05 T, 200 kHz and (b) 0.05 T, 1 MHz.

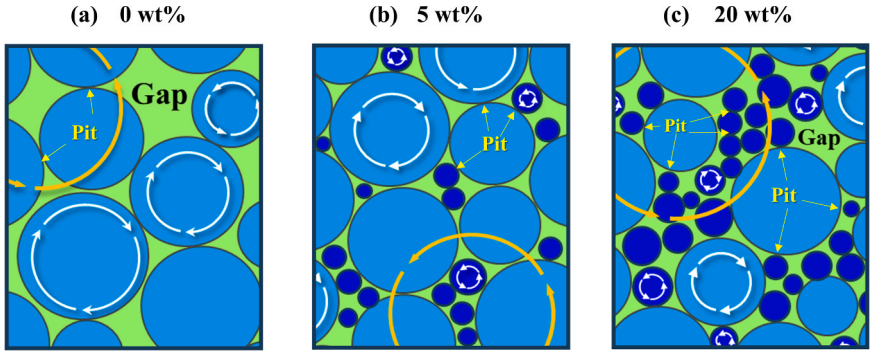

Fig. 12. Schematic illustration of the influence of $Fe_{50}Ni_{50}$ doping on densification and magnetic loss mechanisms of DSMCs.

improvements in magnetic properties. The 5 wt% $Fe_{50}Ni_{50}$-doped DSMCs achieves exceptional performance, with $\mu_e \approx 60$ (stable from 1 kHz to 20 MHz) and ultra-low P_{cv} (86 mW/cm^3 at 0.05 T, 100 kHz and 2441 mW/cm^3 at 0.05 T, 1 MHz), surpassing the performance of traditional SMCs. The improvement in magnetic performance is attributed to the effective filling of interstitial voids, which reduces porosity and enhances magnetic coupling between particles. Loss separation analysis revealed that at low $Fe_{50}Ni_{50}$ contents, the reduction in P_h and P_{exc} is driven by increased density, while at higher doping levels, $Fe_{50}Ni_{50}$ particle agglomeration introduces additional pinning sites, leading to an increase in P_h. Loss separation analysis confirmed that at high frequencies, dynamic domain processes become the predominant loss mechanism, shifting the loss mechanism towards P_{exc}. This study provides a deeper understanding of how $Fe_{50}Ni_{50}$ doping influences the structure-property relationship in Fe-based SMCs, offering a scalable solution for high-performance magnetic materials. By balancing the competing effects of domain-wall motion, eddy currents, and interfacial pinning, $Fe_{50}Ni_{50}$ doping enables the development of high-frequency, low-loss magnetic materials with potential applications in advanced power electronics and miniaturized inductive components.

CRediT authorship contribution statement

Changlong Jin: Investigation, Formal analysis, Data curation. **Yanzhou Fan:** Investigation, Data curation. **Min Wang:** Investigation, Data curation, Formal analysis, Methodology. **Dong Li:** Writing – original draft. **Baolong Shen:** Writing – review & editing, Supervision, Project administration, Funding acquisition. **Zhijun Guo:** Writing – review & editing, Methodology, Funding acquisition. **Qiang Luo:** Formal analysis, Supervision. **Qianqian Wang:** Investigation. **Zhe Jia:** Methodology, Investigation. **Jiayi Huang:** Investigation.

Declaration of Competing Interest

The authors declare that they have no known competing financial interests or personal relationships that could have appeared to influence the work reported in this paper.

Acknowledgments

This work was financially supported by the National Key R&D Program of China (No. 2022YFB3804100), the National Natural Science Foundation of China (No. 52231005), the Science Technology Development Program of Yixing (No. C2024002), the Natural Science Foundation of Jiangsu Province (BK20221474). The authors thank the Center for Fundamental and Interdisciplinary Sciences of Southeast University for the support in magnetic domain measurement.

Data availability

Data will be made available on request.

References

[1] Y. Chen, L. Zhang, H. Sun, et al., Enhanced magnetic properties of iron-based soft magnetic composites with phosphate-polyimide insulating layer, J. Alloy. Compd. 813 (2020) 152205.
[2] M. Cai, J. Wang, Q. Wang, et al., Improvement of soft-magnetic properties for Fe-based amorphous alloys with high saturation polarization by stress annealing, Mater. Res. Lett. 11 (7) (2023) 595–603.

[3] Y. Fan, Z. Guo, M. Wang, et al., Phosphating-enhanced Fe-based amorphous soft magnetic composites with ultra-low power loss for efficient electrical energy conversion, Sci. China Phys. Mech. Astron. 68 (10) (2025) 106112.

[4] Y. Fan, C. Jin, M. Wang, et al., Nb microalloying enhances the amorphous forming ability and soft magnetic properties of high B_s Fe-based nanocrystalline alloys, J. Alloy. Compd. 1044 (2025) 184627.

[5] M. Jiang, J. Wang, M. Cai, et al., Improvement of soft magnetic properties for Fe-based amorphous/nanocrystalline alloy by longitudinal magnetic field annealing, J. NonCryst. Solids 650 (2025) 123382.

[6] M. Cai, Z. Guo, L. Li, et al., Obtaining extremely low coercivity of high B_s FeCoBSiCPCu nanocrystalline alloys through modulation of magnetic anisotropy, J. Mater. Sci. Technol. 207 (2025) 105–112.

[7] Y. Ding, W. Liu, R. Cao, et al., Reductive synthesis of Fe@Al_2O_3 micro powders with high permeability and low magnetic loss in the MHz range, J. Magn. Magn. Mater. 579 (2023) 170865.

[8] Z. Cao, Y. Jiang, Y. Tang, et al., Probing the influence of V_2O_5 and SBZKN composite additives on the magnetic characteristics and power loss of low-temperature sintered NiCuZn ferrites, J. Alloy. Compd. 988 (2024) 174184.

[9] T. Wu, T. Zhan, F. Ding, Structural and magnetic properties of gadolinium substituted $Mn_{0.6}Zn_{0.4}Gd_xFe_{2-x}O_4$ (x = 0-0.1) spinel ferrite, J. Magn. Magn. Mater. 571 (2023) 170554.

[10] L. Shi, K. Yao, Composition design for Fe-based soft magnetic amorphous and nanocrystalline alloys with high Fe content, Mater. Des. 189 (2020) 108511.

[11] G. Li, G. Shi, H. Miao, et al., Effects of the gas-atomization pressure and annealing temperature on the microstructure and performance of FeSiBCuNb nanocrystalline soft magnetic composites, Materials 16 (3) (2023) 1284.

[12] Z. Guo, X. Zheng, C. Jin, et al., A new Fe-based nanocrystalline soft magnetic composites with ultra-low core loss and superior DC-bias permeability up to megahertz-frequency, Mater. Today Nano 30 (2025) 100621.

[13] S. Sun, W. Hu, Z. Li, et al., Study on FeSiAl magnetic powder core coated with nano-Y_2O_3 and its influence on magnetic properties, J. Alloy. Compd. 927 (2022) 166911.

[14] M. Tian, J. Xu, S. Yang, et al., Effects of heat treatment and compaction pressure on the microstructure and magnetic properties of core-shell structured FeSiBNbCu/SiO_2 soft magnetic composites, J. Alloy. Compd. 923 (2022) 166394.

[15] P. Wang, Z. Zhu, Y. Chai, et al., Industrial-scale fabrication of FeSiBC cores with balanced soft magnetic properties by transverse magnetic field annealing and mixing of carbonyl iron powder, J. Alloy. Compd. 977 (2024) 173381.

[16] J. Wang, Z. Guo, Q. Zeng, et al., Magnetic properties regulation and loss contribution analysis for Fe-based amorphous powder cores doped with micron-sized FeSi powders, J. Magn. Magn. Mater. 510 (2020) 166931.

[17] C. Jin, Y. Fan, X. Zheng, et al., Optimizing the high-frequency magnetic properties of Fe-based nanocrystalline soft magnetic composites by incorporating carbonyl iron powder, J. Mater. Sci. Mater. Electr. 36 (34) (2025) 2195.

[18] B. Wang, Z. Zhang, J. Shen, et al., Mechanism of adding carbonyl iron powder to enhance the magnetic properties of Fe-Si-B-Cu-Nb nanocrystalline soft magnetic composites, J. Alloy. Compd. 972 (2024) 172812.

[19] G. Shi, M. Li, H. Wang, et al., Effect of the shape and content for added iron powder on properties of nanocrystalline soft magnetic composites, Mater. Today Commun. 39 (2024) 108888.

[20] Y.J. Choi, M.Y. Lee, B.W. Lee, Magnetic property improvement and core-loss reduction of Fe-Si-Cr-based soft magnetic composites with addition of $Fe_{50}Ni$ nanopowder, JOM 75 (4) (2023) 1261–1269.

[21] J.H. Shin, Y.M. Jeong, K.Y. Sohn, et al., A study on the soft magnetic properties and compaction density of Fe-based nanociystalline powder cores mixed with permalloy powders, J. Korean Inst. Met. Mater. 55 (9) (2017) 645–650.

[22] Y.B. Kim, K.Y. Kim, Effects of the addition of permalloy powder on the high-frequency magnetic properties of Fe-based amorphous powder cores, IEEE Trans. Magn. 42 (10) (2006) 2802–2804.

[23] T. Feng, M. Cheng, Y. Li, et al., Enhancing high-frequency soft magnetic performance of Fe-Si-B-Cu-Nb nanocrystalline alloy powder cores via hybridizing with FeNi, Sci. China Phys. Mech. Astron. 68 (9) (2025) 296111.

[24] Z. Chen, X. Liu, X. Kan, et al., Improved soft magnetic properties of $Fe_{83.5}Si_{7.5}B_5Cr_4$ amorphous nanocrystalline powder cores by adding Permalloy, J. Mater. Sci. Mater. Electr. 29 (22) (2018) 19316–19321.

[25] D.S. Shin, J.W. Oh, I.D. Jung, et al., Densification and magnetic properties of injection molded gas- and water-atomized Fe–Si alloys and effect of Fe-10.2 wt% P addition, Met. Mater. Int. 26 (1) (2020) 94–106.

[26] R. Wang, H. Huang, K. Li, et al., Design and evolution of Fe–Si–Al soft magnetic composites doped with carbonyl iron powders: Overcoming the restrictive relation between permeability and core loss, Ceram. Int. 50 (2024) 17861–17872.

[27] F. Hu, Q. Luo, M. Cai, et al., Transformation-mediated and relaxation-assisted macroscopic tensile plasticity with strain-hardening in metallic glass, Nat. Commun. 16 (1) (2025) 10147.

[28] C. Jiang, X. Li, S.S. Ghosh, et al., Nanocrystalline powder cores for high-power high-frequency power electronics applications, IEEE Trans. Power Electron. 35 (10) (2020) 10821–10830.

[29] H. Cheng, L. Zhang, X. Liu, et al., Optimizing soft magnetic performance of fesial cores by tailoring the Al_2O_3/SiO_2 insulating layer in ethanol/aqueous mixed solvents, J. Electron. Mater. 52 (7) (2023) 4895–4904.

[30] J. Wang, X. Liu, C. Lei, et al., Core loss reduction for Fe-6.5wt%Si soft magnetic composites doped with Co element, J. Magn. Magn. Mater. 502 (2020) 166553.

[31] W. Li, H. Yan, Y. Ying, et al., Analysis of the magnetic properties of a silicate-coated spherical FeSiAl-based soft magnetic composite for high-frequency power-applications, Appl. Phys. Lett. 115 (21) (2019) 212401.

[32] Y. Song, S. Zhou, Z. Zhang, et al., Improvement for soft magnetic properties of FeSiBCuNb nanocrystalline powder cores by adding FeNi powder, J. NonCryst. Solids 646 (2024) 123260.

[33] J.G. Yeo, D.H. Kim, Y.J. Choi, et al., Improving power-inductor performance by mixing sub-micro Fe powder with amorphous soft magnetic composites, J. Electron. Mater. 48 (9) (2019) 6018–6023.

[34] C. Chang, J. Guo, Q. Li, et al., Improvement of soft magnetic properties of FeSiBPNb amorphous powder cores by addition of FeSi powder, J. Alloy. Compd. 788 (2019) 1177–1181.

[35] M. Gong, Y. Dong, J. Huang, et al., The enhanced magnetic properties of FeSiCr powder cores composited with carbonyl iron powder, J. Mater. Sci. Mater. Electr. 32 (7) (2021) 8829–8836.

[36] Z. Guo, J. Wang, W. Chen, et al., Crystal-like microstructural Finemet/FeSi compound powder core with excellent soft magnetic properties and its loss separation analysis, Mater. Des. 192 (2020) 108769.

[37] H. Jun Woo, S. Woo Kim, C. Paul Kim, et al., Formation of mixed-powder composites with improved magnetic properties by adding carbonyl iron powders to FeSiCrB amorphous powder, J. Magn. Magn. Mater. 565 (2023) 170181.

[38] B. Li, Z.G. Zheng, H.Y. Yu, et al., Improved permeability of Fe based amorphous magnetic powder cores by adding Permalloy, J. Magn. Magn. Mater. 438 (2017) 138–143.

[39] H.Z. Li, W.S. Cai, G.Z. Zhang, et al., Improved soft magnetic properties of FeSi/FeSiCrBC compound powder core induced by enhanced magnetic coupling, Powder Technol. 442 (2024) 119899.

[40] J. Liu, Y. Dong, P. Wang, et al., Improved high-frequency magnetic properties of FeSiBCCr amorphous soft magnetic composites by adding carbonyl iron powders, J. NonCryst. Solids 605 (2023) 122166.

[41] X. Liu, Z. Zhang, W. Guo, et al., Ultra-low core loss and high permeability Fe-based amorphous soft magnetic composites with ultra-fine FeNi additives, J. Mater. Sci. Mater. Electr. 35 (24) (2024) 1655.

[42] R. Ma, L. Chang, Y. Dong, et al., Magnetic properties of soft magnetic composites fabricated by injection molding of bimodal amorphous $Fe_{73}Si_{11}B_{11}C_3Cr_2$ and crystalline $Fe_{50}Co_{50}$ powders, Powder Technol. 397 (2022) 116986.

[43] J. Shen, B. Wang, L. Cai, et al., Magnetic properties and thermal stability of Fe-based amorphous/carbonyl iron soft magnetic composites, J. Mater. Sci. Mater. Electr. 34 (14) (2023) 1169.

[44] P. Wang, Z. Zhu, J. Liu, et al., Soft magnetic properties regulation of FeSiBC amorphous powders/CIP magnetic powder core with single and double-layer core–shell structure, J. Magn. Magn. Mater. 578 (2023) 170809.

[45] C. Xia, Y. Peng, X. Yi, et al., Improved magnetic properties of FeSiCr amorphous soft magnetic composites by adding carbonyl iron powder, J. NonCryst. Solids 559 (2021) 120673.

[46] Z. Zhu, P. Wang, J. Liu, et al., Magnetic property regulation and mechanism analysis of FeSiBC soft magnetic composites by mixing with FeSiCr or carbonyl iron powder, J. Magn. Magn. Mater. 588 (2023) 171413.

[47] X. Li, H. Yao, Y. Wan, et al., The balance between low core loss, high permeability, and large dc bias performance in FeSiAl cores covered by polydopamine/polyethyleneimine, J. Electron. Mater. 53 (2024) 3128–3142.

[48] H. Tiismus, A. Kallaste, A. Belahcen, et al., Hysteresis measurements and numerical losses segregation of additively manufactured silicon steel for 3D printing electrical machines, Appl. Sci. 10 (18) (2020) 6515.

[49] H. Zhang, K. Wang, Y. Huang, et al., The excess loss analysis of an easy-plane FeSiAl@SiO_2 soft magnetic composite with high permeability, J. Magn. Magn. Mater. 588 (2023) 171471.

[50] S. Vovk, S. Dobák, J. Füzer, et al., Loss separation and thermal studies of Fe/SiO_2/ferrite soft magnetic composites, J. Alloy. Compd. 945 (2023) 169254.